PCCP

Quantitative Kinetics Reveal that Reactions of HO_2 are a Significant Sink for Aldehydes in the Atmosphere and may Initiate the Formation of Highly Oxygenated Molecules via Autoxidation

Journal:	*Physical Chemistry Chemical Physics*
Manuscript ID	CP-ART-02-2024-000693.R2
Article Type:	Paper
Date Submitted by the Author:	12-May-2024
Complete List of Authors:	Gao, Qiao; Guizhou Minzu University Shen, Chuanyang; University of California Zhang, Haofei; University of California Long, Bo; Guizhou Minzu University Truhlar, Donald; University of Minnesota

SCHOLARONE™
Manuscripts

Quantitative Kinetics Reveal that Reactions of HO_2 are a Significant Sink for Aldehydes in the Atmosphere and may Initiate the Formation of Highly Oxygenated Molecules via Autoxidation

Qiao Gao[a], Chuanyang Shen[b], Haofei Zhang*[b], Bo Long*[a,c] Donald G. Truhlar[d]*

[a]School of Physics and Mechatronic Engineering, Guizhou Minzu University, Guiyang 550025, China

[b]Department of Chemistry, University of California, Riverside, California, 92507, USA

[c]College of Materials Science and Engineering, Guizhou Minzu university, Guiyang 550025, China

[d]Department of Chemistry, Boston College, Chestnut Hill, Massachusetts 02467, United States

[d]Department of Chemistry, Chemical Theory Center, and Minnesota Supercomputing Institute, University of Minnesota, Minneapolis, Minnesota 55455-0431, USA

ABSTRACT: Large aldehydes are widespread in the atmosphere and their oxidation leads to secondary organic aerosols. The current understanding of their chemical transformation processes is limited to hydroxyl radical (OH) oxidation during daytime and nitrate radical (NO_3) oxidation during nighttime. Here, we report quantitative kinetics calculations of the reactions of hexanal ($C_5H_{11}CHO$), pentanal (C_4H_9CHO), and butanal (C_3H_7CHO) with hydroperoxyl radical (HO_2) at atmospheric temperatures and pressures. We find that neither tunneling nor multistructural torsion anharmonicity should be neglected in computing these rate constants; strong anharmonicity at the transition states is also important. We find rate constants for the three reactions in the range $3.2 – 7.7 \times 10^{-14}$ cm^3 $molecule^{-1}$ s^{-1} at 298 K and 1 atm, showing that the HO_2 reactions can be competitive with OH and NO_3 oxidation under some conditions relevant to the atmosphere. Our findings reveal that HO_2-initiated oxidation of large aldehydes may be responsible for the formation of highly oxygenated molecules via autoxidation. We augment the theoretic studies with laboratory flow-tube experiments using an iodide-adduct time-of-flight chemical ionization mass spectrometer to confirm the theoretical predictions of peroxy radicals and the autooxidation pathway. We find that the adduct from $HO_2 + C_5H_{11}CHO$ undergoes a fast unimolecular 1,7-hydrogen shift with a rate constant of 0.45 s^{-1}. We suggest that the HO_2 reactions make significant contributions to the sink of aldehydes.

*Corresponding authors E-mail: wwwltcommon@sina.com (Bo Long), haofei.zhang@ucr.edu (Haofei Zhang), truhlar@umn.edu (Donald G. Truhlar)

1 INTRODUCTION

Aldehydes are released into the atmosphere by direct emission from biogenic and anthropogenic sources,[1-6] and they can be also formed by oxidation of volatile organic compounds (VOC) such as alkanes, alkenes, and alcohols.[7,8] Aldehydes play important roles in the atmosphere, including the formation of secondary organic aerosol (SOAs),[9-11] ozone,[12-17] and free radicals such as hydroxyl radical (OH) and hydroperoxyl radical (HO_2); and the reactions of aldehydes impact the atmospheric oxidation capacity.[9] Therefore, it is important to elucidate atmospheric chemistry of aldehydes.

Aldehydes are understood to undergo photolysis[18] and reaction with OH during the daytime[19] and to mainly react with nitrate radicals (NO_3) during the nighttime – where the OH concentration is very low (< 10^4 molecules/cc)[20-22] and there is no photolysis.[23] Previous investigations have shown that some small aldehydes[24-29] and ketones[30] can react with HO_2. The initial reaction proceeds by forming an adduct between HO_2 and the aldehyde or ketone as in $HO_2 + HCHO \rightarrow HOCH_2OO$ or $HOOCH_2O$. However, studies of the kinetics of HO_2 reactions with aldehydes are limited to small aldehydes such as formaldehyde and acetaldehyde, with estimated rate constants on the order of 10^{-14} cm^3 $molecule^{-1}$ s^{-1}.[28,29,31,32] It is unknown whether similar reactions can occur as rapidly even more rapidly for heavier aldehydes.

Atmospheric concentrations of HO_2 have been reported as high as 1.4×10^8 molecule/cc during the daytime and 3.7×10^7 molecules/cc during the nighttime.[33,34] These concentrations are much higher than those of OH, raising the question of whether HO_2 oxidation may be an important sink for aldehydes. Recently, the RO_2 species produced by OH oxidation of large aldehydes (e.g., hexanal and decanal) have been shown to undergo a hydrogen shift followed by O_2 addition (widely referred to as "autoxidation"[35-40]), leading to the formation of highly oxygenated molecules (HOMs) that can contribute appreciably to SOA formation because of their low volatility.[41-44] If HO_2 reacts rapidly enough with larger aldehydes, they could provide another SOA source in the atmosphere.

In the present work, we carry out quantitative kinetic calculations on the reactions (R1–R3 in **Scheme 1**) of hexanal ($C_5H_{11}CHO$), pentanal (C_4H_9CHO), and butanal (C_3H_7CHO) with HO_2

at atmospheric temperatures and pressures. These aldehydes are studied mainly because they have been observed as major aldehydes in polluted urban atmosphere with high concentrations on the order of 10^{10} molecules/cc.[7,16,45,51] We further explore the hydrogen shifts to the RO_2 group of the adduct peroxy radicals (reactions R4–R6 in **Scheme 1**, which produce $QCH(OH)CH_2OOH$ species). Finally, we report experimental measurements of the key gas-phase products to support the theoretical results for the $HO_2 + C_5H_{11}CHO$ and $HO_2 + C_4H_9CHO$ reactions.

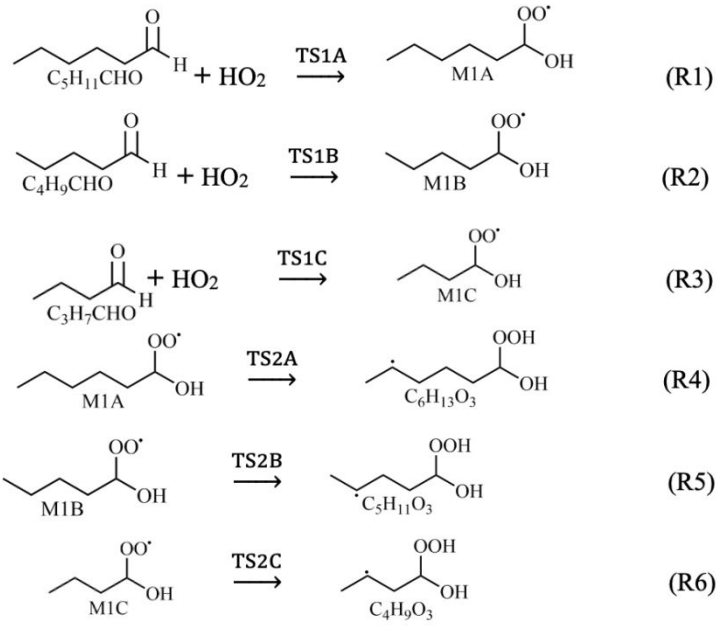

Scheme 1. Reactions and the names of the adducts (prefix M) and lowest-energy conformers of the transition states (prefix TS)

In order to calculate accurate rate constants, our calculations include potential energy surfaces based on high-level electronic structure calculations and a density functional validated against them, anharmonicity effects on zero-point vibrational energies, multiple conformers, variational determination of the transition states, multidimensional tunneling, and pressure effects.

2 METHODS

2.1 Electronic structure methods

We use standard acronyms for electronic structure methods and basis sets, which are explained

with references in **Table S1** (Tables and figures with a prefix S are in the Electronic Supplementary Information (ESI)).

We performed both coupled cluster calculations and density functional calculations. The CC/TZ-F12// method has been shown previously to be reliable for the reactions of small aldehydes with HO_2.[29] But because the systems in this paper have strong correlation, and the coupled cluster calculations are not converged with respect to excitation level or basis set, it is not certain that the coupled cluster calculations are more accurate than the density functional calculations. Nevertheless, we nominally treat the coupled cluster calculations as the higher level (HL) and the density functional calculations as the lower level (LL), and their deviation is a measure of the reliability of either or both. We used calculations with the density functional M06-2X[52] and the MG3S[53] basis set to optimize the geometries and calculate the frequencies of the stationary points in reactions R1–R6 and to calculate the minimum energy paths[54] that connect reactants to products. Coupled cluster calculations[55,56] by CCSD(T)-F12a/cc-pVTZ-F12//M06-2X/MG3S and CCSD(T)-F12a/cc-pVDZ-F12//M06-2X/MG3S (to be denoted respectively as CC/TZ-F12// and CC/DZ-F12// in the rest of the article) were used to perform single-point energy calculations to improve the relative energies of stationary points.

The dynamics calculations involve both levels. The HL electronic structure method is CC/TZ-F12// for reactions R1-R6. Based on comparisons with the HL calculations (see **Tables S6** and **S7**), the density functionals chosen for the LL calculations are M11-L[57] for reactions R1–R3 and MN15-L[58] for reactions R4–R6. The mean unsigned deviation of the LL calculations from the HL ones are 0.8 kcal/mol for R1–R3 (averaged over three classical barrier heights and three enthalpies of activation) and 1.7 kcal/mol for R4–R6 (averaged over three enthalpies of activation and three enthalpies of reaction. The basis set for all LL calculations is MG3S.[53]

2.2 Vibrational frequencies

The calculated harmonic vibrational frequencies were scaled to improve the zero-point vibrational energies. We used two different methods for scaling. The first uses the standard scale factor obtained by optimizing against a database of experimental zero-point vibrational

energies.[59] The standard scale factor for M06-2X/MG3S is 0.970 (see **Table S2**). The second uses the specific-reaction-parameter scale factor[60-63] obtained by hybrid degeneracy-corrected second-order vibrational perturbation theory (HDCVPT)[64-66] to compute anharmonic zero-point vibrational energies for reactants and transition states at the MPW1K/MG3S[53,67] level (see **Table S3**). More details of this method are discussed in our previous work.[60,63]

2.3 Kinetics methods for high-pressure-limit rate constants

Reactions R1–R3 are calculated in two steps. The first step is to calculate the high-pressure limit (HPL); the second step is to calculate the falloff effect, i.e., the lowering of the rate constant as a function of decreasing pressure. Reactions R4-R6 are calculated only in the HPL.

The HPL rate constants were calculated by using dual-level[68-73] multistructural[74] canonical variational transition state theory (MS-CVT)[75] with small-curvature tunneling (DL-MS-CVT/SCT),[76] as used previously.[77] The dual-level strategy combines conventional transition state theory at the higher level (HL) of electronic structure theory[78] with MS-CVT/SCT at the lower level (LL):

$$k = k^{\mathrm{DL}}_{\mathrm{MS-CVT/SCT}}(T) = F^{\mathrm{MS-T,LL}}_{\mathrm{fwd}} \kappa^{\mathrm{LL}}_{\mathrm{SS-SCT}} \Gamma^{\mathrm{LL}}_{\mathrm{SS-CVT}} k^{\mathrm{HL}}_{\mathrm{SS-TST}}(T) \quad (1)$$

where k is the HPL rate constant of the bimolecular reaction; $k^{\mathrm{DL}}_{\mathrm{MS-CVT/SCT}}$ is the bimolecular rate constant calculated by using DL-MS-CVT/SCT with the lowest-energy conformer of the reactant and the lowest-energy conformer of the transition state (see **Figure 1**); $\kappa^{\mathrm{LL}}_{\mathrm{SS-SCT}}$ is the tunneling transmission coefficient calculated by using small-curvature tunneling via the lowest-energy conformer of the transition state from the pre-reactive complex to the corresponding adduct. That is the tunneling calculation assumes that collisional stabilization occurs in the entrance van der Waals well (C1A, C1B, C1C), resulting in a Boltzmann energy distribution in that well; $\Gamma^{\mathrm{LL}}_{\mathrm{SS-CVT}}$ is the recrossing effect corresponding to $\kappa^{\mathrm{LL}}_{\mathrm{SS-CVT}}/\kappa^{\mathrm{LL}}_{\mathrm{SS-TST}}$ by using the single-structural canonical variational transition state theory and transition state theory and the lowest-energy conformer of the transition state; and $k^{\mathrm{HL}}_{\mathrm{SS-TST}}$ is the single-structural conventional transition state theory rate constant without tunneling for the most transition state;

$F_{\mathrm{fwd}}^{\mathrm{MS-T,LL}}$ is the multistructural torsional anharmonicity factor, which includes the contributions from all the conformational structures of reactants, transition states, and intermediates (listed in in **Table S4**), as calculated by the coupled-potential multistructural torsion (MS-T) method.[79-83] It is computed by

$$F_{\mathrm{fwd},}^{\mathrm{MS-T}} = \frac{F_{\mathrm{TS}}^{\mathrm{MS-T}}}{F_{Re}^{\mathrm{MS-T}}} \quad (2)$$

$F_{\mathrm{X}}^{\mathrm{MS-T}}$is the multistructural torsional anharmonicity factor of species X, where X is a reactant (Re) or a transition state (TS), and it equals the ratio of the MS-T partition function to the single-structure harmonic partition function.

In the DL-MS-CVT/SCT calculations, $k_{\mathrm{SS-TST}}^{\mathrm{HL}}$ was computed by using the specific reaction parameter scale factor in **Table S3**, while all the other parameters were calculated by using the standard scale factor in **Table S2**. The bimolecular rate constants for R1–R3 are called k_{R1}, k_{R2} and k_{R3}, and the unimolecular rate constants for R4– R6 re called k_{1u}, k_{2u}, and k_{3u}. The computational details for all the rate constants in the Supporting Information

2.4 Kinetics methods for pressure-dependent rate constants

The falloff effect, defined as the rate constant at infinite pressure divided by the rate constant at a given finite pressure, was computed for reactions R1–R3 by using the system-specific quantum Rice−Ramsperger−Kassel (SS-QRRK) theory[79,80,84-86] and also by using the energy-grained master equation (ME/RRKM)[87-89] with the direct diagonalization method. In the ME/RRKM calculations, the microcanonical rate constants were computed by using Rice-Ramsperger-Kassel-Marcus (RRKM) theory[90] with Eckart tunneling[91,92,93] at the CC/TZ-F12//level. We considered two steps for HO_2 + $C_5H_{11}CHO$/C_4H_9CHO/C_3H_7CHO→C1A/C1B/C1C→ M1A/M1B/M1C in ME/RRKM calculations. In the pressure-dependent rate constant calculations, we used the exponential gap model[94] for energy transfer with $<\Delta E>_{\mathrm{down}}$ equal to 300 cm^{-1}, where $<\Delta E>_{\mathrm{down}}$ is the average energy transferred in a collision in which the energy in the reacting molecule decreases. The collision rate was calculated by the Lennard−Jones model with the Lennard−Jones parameters given in **Table S5**.

2.5 Software

Conformers of each species were generated by the *MSTor-2017* code[95-97] by rotating all the dihedral angles of an optimized geometry. Density functional calculations were performed using the *Gaussian 16* program.[98] The coupled cluster calculations were performed using *Molpro 2019*.[99] Rate constants were calculated using *Polyrate 2017-C*[100] and *Gaussrate 2017*-B.[101] The ME/RRKM and master equation calculations were carried out with the MESS program.[102]

2.6 Laboratory studies

To verify the computational results, laboratory experiments were performed in a flow tube reactor (Quartz, volume ~2.1 L) to study the HO_2 + hexanal/pentanal reactions at 295 K and 10% relative humidity. The total flow rate in the reactor was 2.1 L/min, corresponding to a residence time of approximately 1 min. The details of the flow tube reactor setup and operation have been described previously.[103,104] Briefly, a clean-air generator (Aadco Instruments) was used to provide clean dry air. Hexanal (99%, ACROS organics) was injected into the reactor using a syringe pump with an initial concentration of ~470 ppb. We used alkene (i.e., tetramethylethylene and a-pinene, concentrations ~ 1 ppm) ozonolysis to generate OH and injected high concentrations of methanol (5–240 ppm) to convert the produced OH into HO_2.[105] Given the experimental conditions, we estimated that the HO_2 concentrations in the flow tube reactor range from 0.2 to 0.8 ppb and the total RO_2 concentrations range from 20 to 50 ppb, based on kinetic box model simulations using the Master Chemical Mechanism (MCMv3.3.1). Under these conditions, the RO_2 produced by the aldehyde oxidation are mainly consumed by RO_2 + RO_2 reactions, with RO_2 + HO_2 a minor but still detectable pathway, due to the faster reaction rate constant. Because OH is inevitably co-generated, the oxidation conditions correspond to mixed OH and HO_2; however, the distinct reaction mechanisms (i.e., H-abstraction by OH vs. adduct formation by HO_2) make it possible to differentiate the products from the two pathways in most cases. The oxidation products were analyzed in real time using an iodide-adduct time-of-flight chemical ionization mass spectrometer with a mass resolution ($m/\Delta m$) of ~5000 (I-CIMS, Aerodyne Research Inc.).[103,106,107] The I-CIMS is known to be sensitive for

multifunctional organic compounds.[108-111] The flow tube reactor was directly interfaced with the I-CIMS inlet, allowing probing of HO_2 and oxidation products with little wall loss.

3 RESULTS AND DISSCUSSION

3.1 The formation of RO_2 adducts in the HO_2 + aldehyde reactions

The reaction between HO_2 and $C_5H_{11}CHO$ results in the formation of adduct M1A ($C_6H_{13}O_3$) by transition state TS1A and its conformers, as shown in **Scheme 1**. The reaction is similar to those the HO_2 + HCHO, HO_2 + CH_3CHO, and HO_2 + CF_3CHO reactions.[29] However, there are 27 distinguishable conformers for $C_5H_{11}CHO$ and 33 for the HO_2 + $C_5H_{11}CHO$ transition state (with the lowest-energy one being TS1A – see **Table S4**), so the reactions studied here are more complicated. The reaction mechanisms of the HO_2 + C_4H_9CHO and HO_2 + C_3H_7CHO reactions are similar to that of the HO_2 + C_5H_9CHO reaction. The numbers of distinguishable structures of C_4H_9CHO, C_3H_7CHO, TS1B, and TS1C are 9, 3, 16, and 9, respectively (see **Table S4**).

All enthalpies in this article are given for temperature of 0 K, at which the enthalpy is equal to the potential energy of the lowest-energy structure (of a stable species or transition state) plus the zero-point energy. The lowest-energy conformers for the reactant, the transition state, and the adduct are illustrated in **Figure 1** for reactions R1–R3, where enthalpy of reaction is defined as enthalpy of the lowest-energy product conformer minus the enthalpy of the lowest-energy reactant conformer, and enthalpy of activation defined as enthalpy of the lowest-energy transition state conformer minus the enthalpy of the lowest-energy reactant conformer. The calculated enthalpy of activation for R1 with standard vibrational-frequency scaling is –1.67 kcal/mol, which is similar to the values of –1.03, –1.17, and –1.86 kcal/mol in the HO_2 reaction with HCHO, CH_3CHO, and C_2H_5CHO, respectively.[28, 29] This shows that the carbon chain length in aldehydes has only a minor influence on the enthalpies of activation for reaction with HO_2.

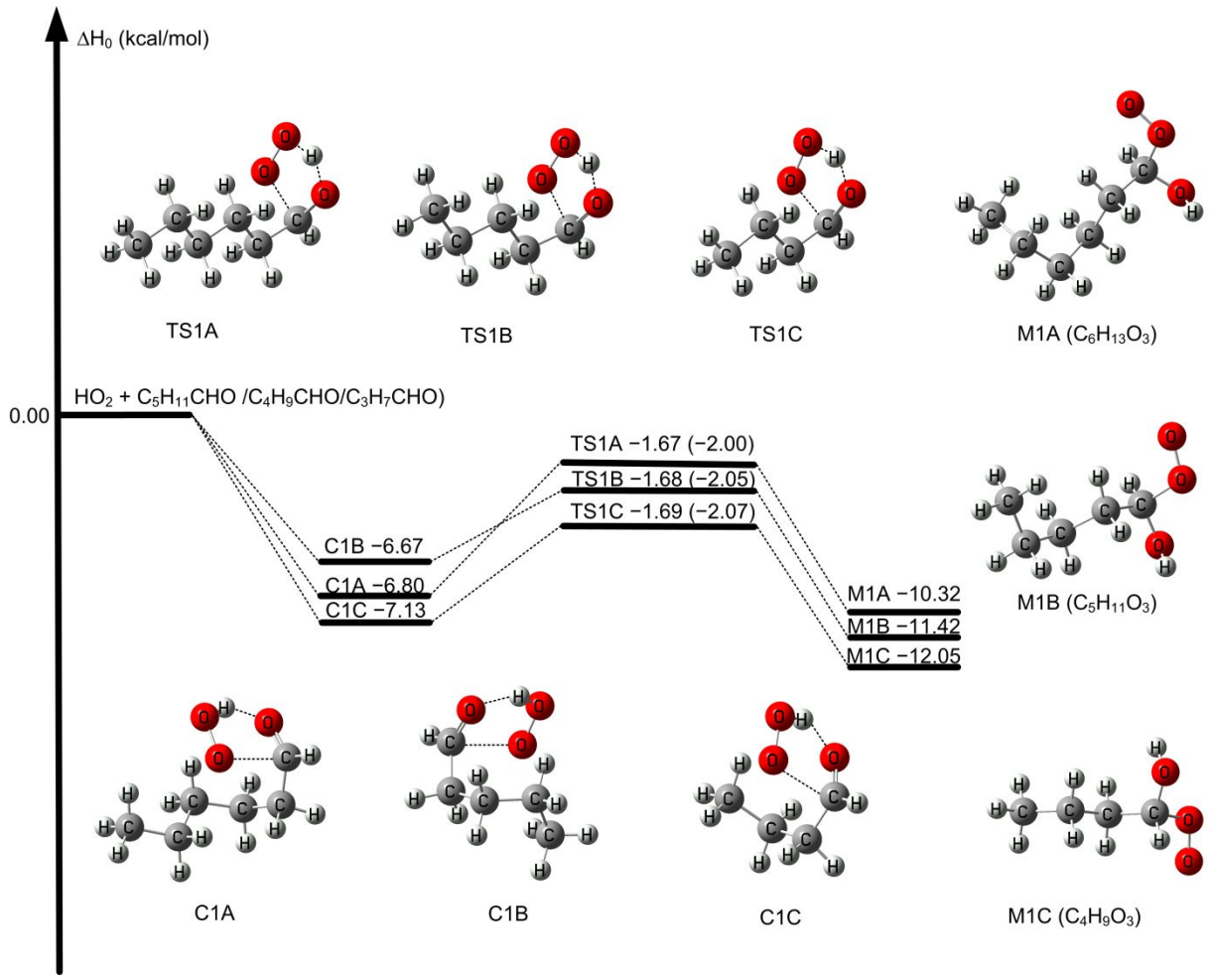

Figure 1. The relative enthalpy profile of the HO_2 + $C_5H_{11}CHO$, HO_2 + C_4H_9CHO, and HO_2 + C_3H_7CHO reactions at the CC/TZ-F12//level. All enthalpies in this article are given at 0 K. For the transition states, the result with the standard vibrational scale factor is given first, followed (in parentheses) by the result with the specific reaction parameter for the vibrational scale factor. For the bound species, the results are obtained with the standard vibrational scale factor.

We used two different methods for scaling vibrational frequencies to account for anharmonicity and systematic errors in the density functional calculations. The standard scale factor[59] for M06-2X /MG3S is 0.970 (see **Table S2**). In the standard procedure, the calculated vibrational frequencies of all the species are scaled by the same factor, which is deemed appropriate for stable molecules. However, the anharmonicity at transition states is known to often be quite different from that of stable molecules.[29,60 ,62,63,112-116] We calculated M06-2X/MG3S specific reaction parameter scale factors to be 0.967, 0.970 and 0.967 for HO_2,

$C_5H_{11}CHO$, and TS1A, respectively as listed in **Table S3**. This shows that the standard scale factor is sufficient for the reactant $C_5H_{11}CHO$, while the standard scale factor is not sufficient for HO_2 and the transition state TS1A. As seen in **Figure 1**, using the specific reaction parameters reduces the enthalpy of activation for TS1A by 0.33 kcal/mol to -2.00 kcal/mol.

Figure 1 shows slightly larger specific-reaction-parameter lowering for TS1B and TS1C; it shows that the enthalpies of activation of the HO_2 + C_4H_9CHO and HO_2 + C_3H_7CHO reactions with specific reaction parameters for vibrational frequency scaling are -2.05 and -2.07 kcal/mol, respectively, in which is close the value of 0.33 kcal/mol for TS1A.

The calculated HO_2 oxidation pathway is supported by the flow tube experiments. The exemplified mass spectra from the experiments are illustrated in **Figure S1**. Although the peroxy radical M1A ($C_6H_{13}O_3$) was not directly observed owing to the isotopic interference caused by the large peak at $C_6H_{12}O_3$ (from OH oxidation of $C_5H_{11}CHO$), its bimolecular reaction product ($C_6H_{14}O_3$) via the M1A + HO_2 reaction was found to be present and increases with the HO_2 intensity (**Figure 2A**). (Because OH oxidation of hexanal proceeds via H-abstraction, all the $C_6H_{14}O_x$ products must be from the HO_2 oxidation pathway.) To rule out the possibility that tetramethylethylene (C_6H_{12}) oxidation might form $C_6H_{14}O_3$, α-pinene ozonolysis was used instead in some experiments to verify that $C_6H_{14}O_3$ was formed from hexanal. Mass spectral comparisons were carefully performed to verify that the $C_6H_{14}O_x$ products are not present in pure α-pinene ozonolysis. Because OH oxidation products (such as $C_6H_{12}O_3$) should decrease with increasing HO_2, as OH is converted to HO_2, the increasing trend of $C_6H_{14}O_3$ with HO_2 unambiguously suggests that it is formed from the hexanal + HO_2 pathway. Due to the abundant HO_2 in the reactor, the formed peroxy radical M1A ($C_6H_{13}O_3$) rapidly reacted with HO_2 to produce $C_6H_{14}O_3$ (**Figure S1**). **Figure 2B** shows that the analogous product ($C_5H_{12}O_3$) was also observed from pentanal + HO_2, suggesting that the HO_2 adduct reaction is likely a generic process for aldehydes.

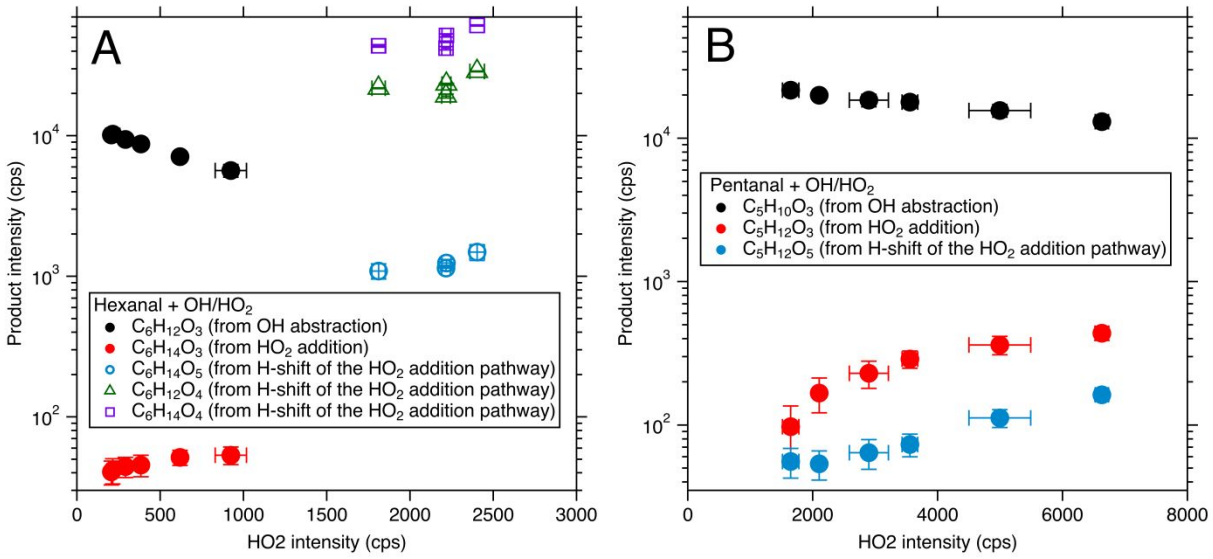

Figure 2. Major oxidation products from (A) hexanal + OH/HO_2 and (B) pentanal + OH/HO_2 as functions of measured HO_2 intensities. A decreasing trend may suggest products from OH oxidation and an increasing trend may suggest products from HO_2 oxidation. In (A), because tetramethylethylene may form identical chemical formulas with some hexanal oxidation products, some data were collected using α-pinene ozonolysis (with HO_2 intensities < 1000 cps). The error bars represent standard deviation.

3.2 Hydrogen shift reactions of the HO_2 adducts

We carried out CC/DZ-F12// calculations to explore all possible hydrogen shift pathways of the adducts M1A, M1B, and M1C, **Figure S2** shows that the 1, 7 H-shift of M1A ($C_6H_{13}O_3$) has the lowest calculated enthalpy of activation. This enthalpically most favored hydrogen shift proceeds through transition state structure TS2A to yield product M2A. The adduct M1A has 256 distinguishable structures, but the transition state TS2A has only 2; this results in a multistructural torsion anharmonicity factor that lowers the reaction rate by a factor of 0.18 at 300 K and a factor of 0.34 at 200 K.

Increasing the level of calculation of the enthalpy of activation to CC/TZ-F12// changes the enthalpy of activation from 17.91 to 17.13 kcal/mol, as shown in **Figure 3**. We used the CC/DZ-F12// level for the HL kinetics of reactions R4–R6.

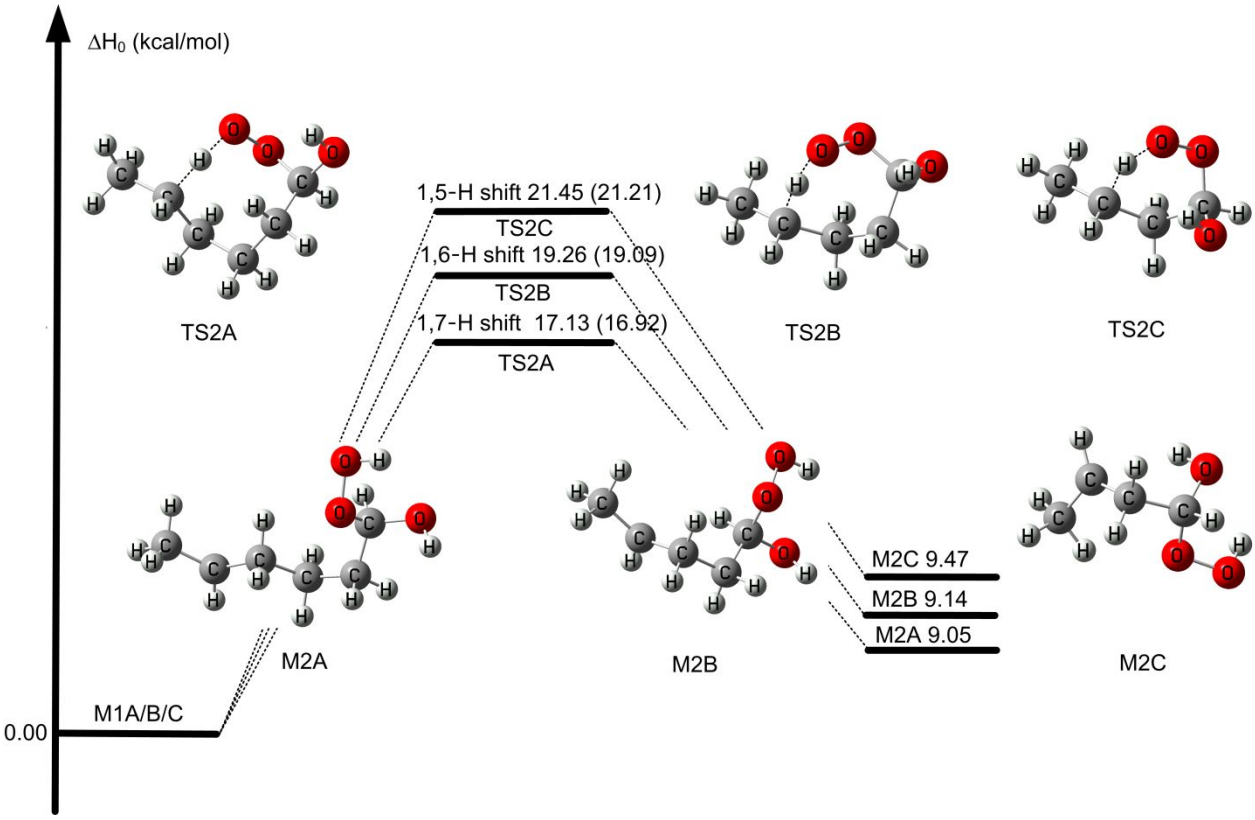

Figure 3. The relative enthalpy profile of the H-shifts of M1A, M1B, and M1C at the CC/TZ-F12//level with the scale factor by the standard method and with specific reaction parameter scale factor in parentheses, respectively.

Figures S3 and **S4** show the possible H-atom migration pathways of the hydrogen-shift reactions of adducts M1B ($C_5H_{11}O_3$) and M1C ($C_4H_9O_3$). CC/DZ-F12// calculations indicate that the lowest-enthalpy path for M1B is a 1,6-H-shift via TS2B to form M2B with an enthalpy of activation of 19.42 kcal/mol, and that for M1C is a 1,5-H-shift via TS2C to form M2C with an enthalpy of activation of 21.63 kcal/mol. The numbers of distinguishable structures for M1B, M1C, TS2B, and TS2C are 101, 31, 2, and 2 (see **Table S4**). For the kinetics of the H-shift processes of the HO_2 adducts, we only studied the 1, 7-H-shift of M1A, the 1, 6-H-shift of M1B, and the 1, 5-H-shift of M1C because these reactions have the lowest enthalpies of activation.

Figure 3 shows that the specific reaction parameters for scaling vibrational frequencies reduce the enthalpies of activation for TS2A, TS2B, and TS2C by 0.21, 0.17 and 0.24 kcal/mol respectively.

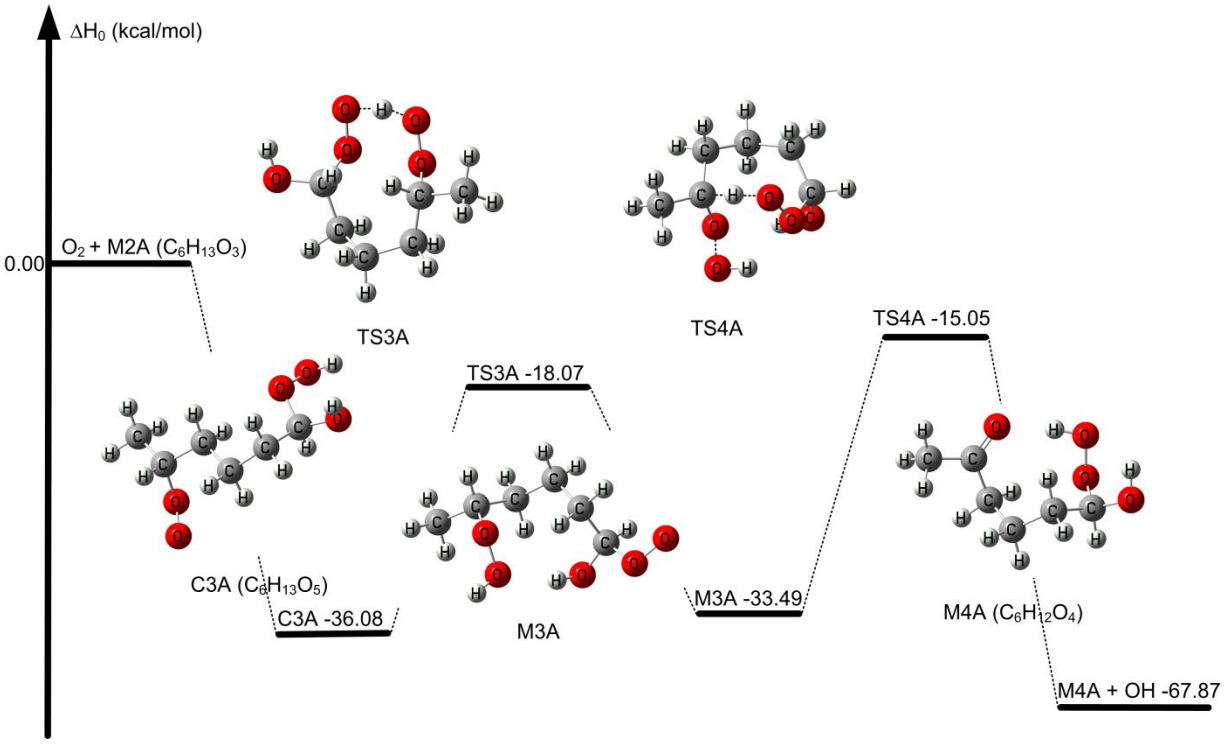

Figure 4. The relative enthalpy profile of the H-shift reaction of the C3A ($C_6H_{13}O_5$) at the CC/DZ-F12//level with the scale factor by the standard method.

3.3 Autooxidation

The product (M2A) of the 1,7-H-shift of M1A can add an O_2 molecule to form the peroxy radical C3A ($C_6H_{13}O_5$), as shown in **Figure 4**. All possible H-atom migration pathways of C3A are described in **Figure S5**, and we find that the lowest-energy pathway is a 1,9-H-shift via TS3A to form M3A with an enthalpy of activation of 18.01 kcal/mol (**Figures 4** and **S5**), where the hydrogen atom of the HO_2 group in C3A is transferred unimolecular to the terminal oxygen atom of OO group, leading to the formation of M3A (see **Figures 4** and **S5**). Subsequently, the intermediate M3A undergoes a 1, 7-H-shift to yield the closed-shell hydroperoxide product M4A ($C_6H_{12}O_4$) and release hydroxyl radical (OH) with an enthalpy of activation of 18.44 kcal/mol (**Figure S6**).

Figure S6 shows that the next most feasible reaction channel of intermediate M3A a 1, 6-H shift to yield M4B with an enthalpy of activation of 22.12 kcal/mol. Addition of O_2 to M4B yields the peroxy radical C5A ($C_6H_{13}O_7$), which further forms M5A ($C_6H_{12}O_6$) + OH or M5B

($C_6H_{13}O_7$). All-possible H-atom migration pathways of C5A are shown in **Figure S7**.

The autoxidation processes are also supported by the experimental results, as shown in **Figure 2**. In the case of hexanal + HO_2, the products from bimolecular and unimolecular reactions of C3A ($C_6H_{13}O_5$) were observed (see **Scheme 2**), including $C_6H_{14}O_5$, $C_6H_{12}O_4$, and $C_6H_{14}O_4$. Here, $C_6H_{14}O_5$ is likely a product from C3A + HO_2; $C_6H_{14}O_4$ is likely formed from C3A + RO_2; and $C_6H_{12}O_4$ may come either from C3A + RO_2 or from C3A unimolecular H-shift and subsequent self-termination (i.e., M4A). All these products were found experimentally to increase with HO_2, suggesting that they are from the hexanal + HO_2 pathway, consistent with the calculation results. The lack of further autoxidation products may be due to slow H-shifts and high concentrations of reacting HO_2 and RO_2, terminating the reactions. Similar products and trends were also observed on the pentanal experiments.

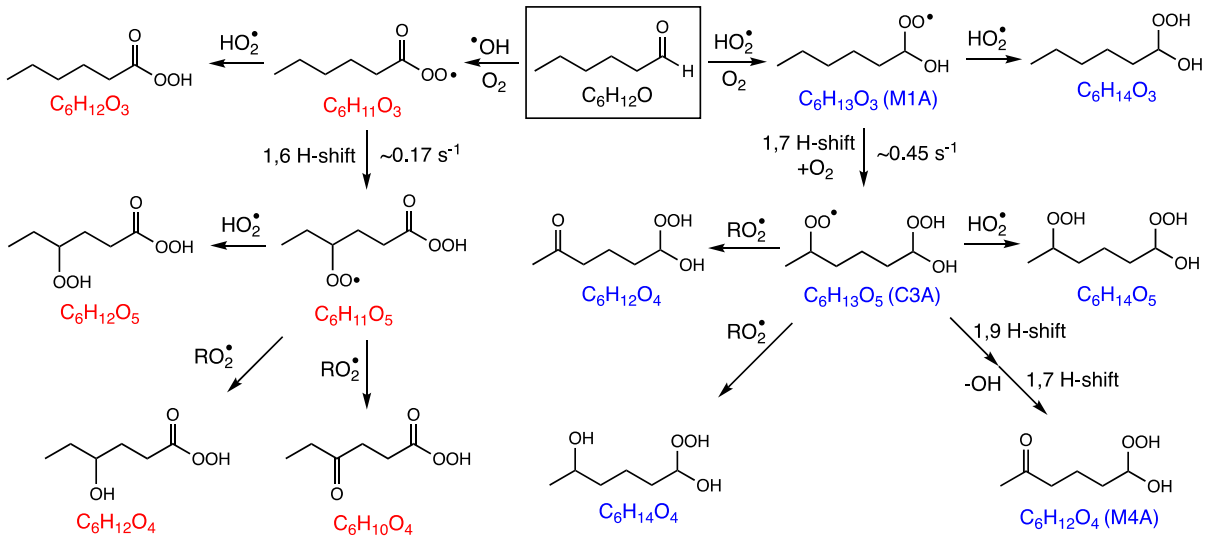

Scheme 2. The simplified reaction mechanisms in the HO_2/HO + $C_5H_{11}CHO$ reactions. The 1,6-H-shift rate constant in the OH oxidation pathway is based on the recent work if Barua et al.;[44] the 1,7-H-shift rate constant in the HO_2 oxidation pathway is from this work.

3.4 High-pressure rate constants

Table 1 gives the HPL rate constants (k_{R1},k_{R2},and k_{R3}) for the HO_2 reactions with $C_5H_{11}CHO$, C_4H_9CHO, and C_3H_7CHO reactions over the temperature range from 190 to 350 K, with additional details provided in **Tables S8–S10**. These rate constants are fitted using the following four parameter function[80,117,118] in the temperature range from 190 to 350 K:

$$k = A\left(\frac{T+T_0}{300}\right)^n exp\left[-\frac{E(T+T_0)}{(T^2+T_0{}^2)}\right] \quad (2)$$

where *R* is the gas constant, T is temperature in K, and the fitting parameters are listed in **Table S14**. The temperature dependent Arrhenius activation energies are computed from the fits by

$$E_a = -R\frac{d\,ln\,k}{d\left(\frac{1}{T}\right)} \quad (3)$$

and are given in **Tables S8–S10**.

Table 1. High-pressure-limit rate constants (cm^3 $molecule^{-1}$ s^{-1}) for reactions R1–R3

$T(K)$	k_{R1} $C_5H_{11}CHO$	k_{R2} C_4H_9CHO	k_{R3} C_3H_7CHO
190	6.40×10^{-13}	1.26×10^{-12}	9.58×10^{-13}
210	3.07×10^{-13}	5.99×10^{-13}	4.49×10^{-13}
230	1.72×10^{-13}	3.33×10^{-13}	2.46×10^{-13}
250	1.08×10^{-13}	2.07×10^{-13}	1.52×10^{-13}
270	7.33×10^{-14}	1.40×10^{-13}	1.02×10^{-13}
290	5.33×10^{-14}	1.00×10^{-13}	7.35×10^{-14}
298	4.75×10^{-14}	8.93×10^{-14}	6.53×10^{-14}
310	4.08×10^{-14}	7.61×10^{-14}	5.56×10^{-14}
330	3.25×10^{-14}	6.01×10^{-14}	4.44×10^{-14}
350	2.68×10^{-14}	4.91×10^{-14}	3.60×10^{-14}

The calculated HPL rate constants of k_{R1}, k_{R2}, and k_{R3} have a negative temperature, leading to negative Arrhenius activation energies in the range -2.1 to -3.1 kcal/mol. The negative temperature dependence of the HPL rate constants was also observed in the reactions of small-sized aldehydes with HO_2. [29] At 298 K, **Table 1 s**hows HPL rate constants in the range 4.8×10^{-14} to 6.5×10^{-14} cm^3 $molecule^{-1}$ s^{-1}; these are slightly faster than the rate of HO_2 + CH_3CHO.[29]

The 1,7-H-shift reaction of peroxy radical intermediate M1A ($C_6H_{13}O_3$), responsible for the formation of a M2A radical (see **Scheme 2 and Table S11),** has an HPL rate constant at 298 K of 0.45 s^{-1}, which is only 2.6 times slower than that of a aldehydic 1,7-H-shift.[119] In contrast, the peroxy radical intermediate M1B ($C_5H_{11}O_3$) undergoes a 1, 6-H-shift reaction to form a M2B radical with a slow 298 K HPL rate constant of 0.020 s^{-1} (see **Table S12**), and the peroxy radical M1C ($C_4H_9O_3$) undergoes a 1, 5-H-shift reaction to form a M2C radical with a slower 298 K

HPL rate constant of 0.0026 s^{-1} (see **Table S13**). However, although the H-shift rate constant is low for M1B, **Figure 2B** shows that a termination HO_2 oxidation product was observed.

The tunneling is not negligible for any of the six reactions. For example, the small-curvature tunneling transmission coefficients at 190−300 K are in the range of 4.7−1.9, 4.9−1.9, and 4.8−1.9 for R1, R2, and R3, respectively (see **Tables S8–S10**). The tunneling transmission coefficients are even larger at these temperatures for the H-shift reactions, being in the range of 557−20, 769−18, and 3.56×10^5−32 for R4, R5, and R6, respectively (see **Tables S11–S13**).

The multistructural torsional anharmonicity factors are in **Tables S8–S13**. At 190−350 K, they increase the rates by factors of about 1.2, 1.9, and 1.4 for R1, R2, and R3, respectively. However, for R4, R5, and R6, they decrease the rates by factors in the ranges 0.37−0.14, 0.40−0.19, and 0.41−0.24, respectively.

We conclude that neither tunneling nor multistructural torsion anharmonicity should be neglected in computing these rate constants.

The effect on the rate constants of the vibrational frequency scale factors is mainly due to the zero-point energies because of changes in the high-frequency modes. These effects were considered in the HPL rate constants of R1–R3 by using conventional transition state theory to calculate the rate constants at 190−350 K by using both the standard scale factor and specific-reaction-parameter scale factor (see **Tables S15** and **S16**). For reactions R1–R3, the effects respectively vary from 2.2, 2.5, and 2.6 at 190 K to 1.5, 1.6, and 1.6 at 350 K. For reactions R4-R6, the effects respectively vary over 1.89–1.4, 1.7–1.3, and 1.9–1.4 in the same temperature range.

3.5 Pressure-dependent rate constants

We calculated the pressure-dependent rate constants of R1–R3 by using both the SS-QRRK and the ME/RRKM methods; the results are in **Tables S18A–S20B**. We define the falloff factor $f(p)$ as the ratio of HPL rate constant to the pressure-dependent rate constant pressure p, and these are given in **Table S17** for a pressure of 1 bar. The falloff effects from the two methods agree well with each other. For example, **Table S17** shows that the falloff effect for R1 at 1 bar is estimated

by SS-QRRK to increase from 1.04 at 190 K to 1.5 at 298 K and is estimated by ME/RRKM to increase from 1.02 at 190 K to 1.8 at 298 K. Therefore, we only discuss the pressure-dependent rate constants obtained by the SS-QRRK method.

The falloff factors increase as pressure is lowered. The falloff factors at 298 K and 0.1 bar for the three HO_2 reactions are somewhat different from one another: 4.5 for R1 (**Table S18A**) and 2.1 for R2 and R3 (**Tables S18A, S19A, and S20A**). These are similar to previously reported pressure effects in the reactions of HO_2 with small aldehydes,[29] which are 3.8 for HCHO and 1.5 for CH_3CHO at 0.1 bar and 298 K.

Table 2 illustrates the falloff under conditions typical of the upper troposphere. The falloff effects are lower due to the lower temperature; they range from 1.1 to 1.3 for the conditions shown. Results for a greater variety of conditions are given in **Tables S18A**, **S19A**, and **S20A**.

Table 2. SS-QRRK calculations of high-pressure-limit rate constants, pressure-dependent rate constants (both in 10^{-13} cm^3 $molecule^{-1}$ s^{-1}) and falloff factors (unitless)

Reaction		$T = 230\ K$ $p' = 0.316$ bar	$T = 250\ K$ $p' = 0.562$ bar
R1	$p = \infty$	1.72	1.08
	$p = p'$	1.30	0.84
	$f(p')$	1.32	1.28
R2	$p = \infty$	3.33	2.98
	$p = p'$	2.98	1.88
	$f(p')$	1.12	1.10
R3	$p = \infty$	2.46	1.52
	$p = p'$	2.18	1.38
	$f(p')$	1.13	1.10

4 Atmospheric Implications

Next we consider the role of the HO_2 reactions with the three aldehydes as bimolecular sinks for aldehydes and explore the process of autoxidation leading to higher oxidized products formation. Customarily, the primary reactions for these aldehydes are considered to be reactions with OH during daytime and with NO_3 during nighttime. The typical HO_2 concentration, daytime OH concentration, and nighttime NO_3 concentration are estimated to be 1.4×10^8 molecules/cc,[32] 10^6

molecules/cc,[23,120] and 5×10^8 molecules/cc,[121-123] respectively. **Table 3** shows that the reactions of HO_2 with the studied aldehydes are competitive with the OH oxidation of aldehydes during the daytime and with NO_3 oxidation during the nighttime in the atmosphere at 298 K. Thus, the contributions of the HO_2 reactions as sinks for $C_5H_{11}CHO$, C_4H_9CHO, and C_3H_7CHO are not negligible, especially during nighttime.

Table 3. The rate coefficients (in cm^3 $molecule^{-1}$ s^{-1}) at 298 K and 1 bar for the reactions of HO_2, OH, and NO_3 with the three aldehydes and the corresponding atmospheric lifetimes τ (in s).

Compound	$k(HO_2)$	$k(OH)$[124]	$k(NO_3)$[124]	τ_{HO_2}	τ_{OH}	τ_{NO_3}
$C_5H_{11}CHO$	3.22×10^{-14}	3.17×10^{-11}	1.49×10^{-14}	2.2×10^5	3.2×10^4	1.3×10^5
C_4H_9CHO	7.70×10^{-14}	2.99×10^{-11}	1.41×10^{-14}	9.3×10^4	3.3×10^4	1.4×10^5
C_3H_7CHO	5.68×10^{-14}	2.47×10^{-11}	1.12×10^{-14}	1.3×10^5	4.0×10^4	1.8×10^5

[a]For bimolecular reactions, $\tau_R = 1/k[x]$, where k is the bimolecular rate coefficient of HO_2 + RCHO (R = C_5H_{11}, C_4H_9, or C_3H_7) and [x] is the concentration of HO_2, OH, or NO_3 (values are given in the text).

We also calculated the atmospheric lifetimes of the three aldehydes against HO_2 as functions of altitude at 0−15 km (with standard values for the temperature at each altitude); the results are listed in **Table 4** and **Table S21**. These tables show that the reactions of HO_2 with $C_5H_{11}CHO$, C_4H_9CHO, and C_3H_7CHO dominate over the NO_3 reactions with these altitudes at 0−15 km.

Table 4. HO_2 concentration, rate constants, and atmospheric lifetimes with respect to bimolecular reactions as functions of altitude[a]

H (km)	*T* (K)	*p* (bar)	[HO_2] (molecules /cc)	k_{R1} (*T*, *p*) (molecules cm^{-3} s^{-1})	k_{R2} (*T*, *p*) (molecules cm^{-3} s^{-1})	k_{R3} (*T*, *p*) (molecules cm^{-3} s^{-1})	τ_1 (s)	τ_2 (s)	τ_3 (s)
0	290.2	0.1013	1.40×10^{8}	3.81×10^{-14}	8.83×10^{-14}	6.50×10^{-14}	1.87×10^{5}	8.09×10^{4}	1.10×10^{5}
5	250.5	0.4959	4.90×10^{7}	8.02×10^{-14}	1.83×10^{-13}	1.34×10^{-13}	2.54×10^{5}	1.12×10^{5}	1.52×10^{5}
10	215.6	0.2428	8.30×10^{6}	1.97×10^{-13}	4.52×10^{-13}	3.31×10^{-13}	6.12×10^{5}	2.67×10^{5}	3.65×10^{5}
15	198	0.1188	2.30×10^{6}	3.30×10^{-13}	7.97×10^{-13}	5.83×10^{-13}	1.32×10^{6}	5.50×10^{5}	7.46×10^{5}

[a] $\tau_x = \frac{1}{k_{Rx}(T,p)[HO_2]}$ (x = 1, 2, and 3), where $k_{Rx}(T,p)$ is the bimolecular rate constant of HO_2 + $C_5H_{11}CHO$ (x = 1), C_4H_9CHO (x = 2), or C_3H_7CHO (x = 3).

Customary atmospheric chemistry models, especially in less polluted environments, assume that HO_2 serves as the main terminator for RO_2 radicals through HO_2 + RO_2 reactions, forming organic hydroperoxide. In contrast, the present investigations show that HO_2 may initiate the formation of RO_2 radials that are capable of undergoing autoxidation leading to formation of higher oxidized products. In a recent study, RO_2 ($C_6H_{11}O_3$) formed from OH + $C_5H_{11}CHO$[44] was shown to autoxidize at ~ 0.17 s^{-1} and initiate higher oxidized products formation (**Scheme 2**). Here, we show that an analogous process can take place from HO_2 oxidation and produce an RO_2 ($C_6H_{13}O_3$) that can autoxidize at a faster rate constant (~ 0.45 s^{-1}). In the atmosphere, the typical RO_2 bimolecular reaction rate is in the range of 0.01–1 s^{-1} from pristine to polluted regions.[125] This suggests that the RO_2 from HO_2 oxidation of some large-sized aldehydes can autoxidize fast enough to compete with bimolecular RO_2 reactions. We also estimate that the termination products from HO_2 + hexanal are in the range of semi-volatile organic compounds, even with only one step of autoxidation (**Table S22**). Therefore, they may contribute to SOA formation in the atmosphere.

In addition to the simple straight-chain aldehydes investigated in this work, substantial quantities of various other large aldehydes are present in the atmosphere. For example, aldehydes are known to form from oxidation of terpenoid and aromatic hydrocarbons. Many of these aldehydes are oxidized and are even larger than those studied here. The presence of functional groups and longer carbon chains could potentially facilitate RO_2 autoxidation with faster rate

constants than those reported here. If the HO_2 oxidation kinetics is fast enough, this new pathway may be an important sink for those aldehydes and contribute significantly to atmospheric SOA.

5 Concluding remarks

The gas-phase reactions of HO_2 with $C_5H_{11}CHO$, C_4H_9CHO, and C_3H_7CHO have been investigated theoretically and experimentally. The theoretical treatment uses multistructural canonical variational transition state theory (MS-CVT) with small-curvature tunneling and dual-level electronic structure, with the higher level being CC/TZ-F12// and the lower level being M11-L/MG3S. The experimental treatment uses a flow tube reactor and an iodide-adduct time-of-flight chemical ionization mass spectrometer.

The prominence of the process studied here depends on the chemical state of the atmosphere. Our calculated results show that under some conditions relevant to the atmosphere, HO_2 reactions with $C_5H_{11}CHO$, C_4H_9CHO, and C_3H_7CHO can compete well with the corresponding OH and NO_3 oxidation reactions. Subsequently, H-shift reactions of the RO_2 radicals formed in the $HO_2 + C_5H_{11}CHO$ reaction are surprisingly fast, which leads to the formation of M2A ($C_6H_{13}O_3$) and M2B ($C_5H_{11}O_3$) intermediate products. These findings are supported by experiments.

The calculations show that tunneling significantly enhances the rate constants of H-shift reactions, and torsional anharmonicity significantly decreases the rate constants of H-shift reactions. For the $HO_2 + C_5H_{11}CHO$ reaction, the adduct intermediate M1A can lead to autoxidation processes that make higher oxidized products through hydrogen-shift reactions of the formed RO_2.

Data availability

Data for this paper are available in the ESI., which contains scale factors, specific reaction scale factors, Lennard-Jones parameters, the high-pressure limit rate constant, activation energy, fitting parameters for the high-pressure limit rate constants, the calculated multistructural torsional anharmonicity factor, the conventional transition state theory (TST) rate constants, the pressure-dependent rate constants, comparison of the rate constants, volatility estimation of the products, the Cartesian coordinates (Å) of the optimized geometries, absolute energies in hartrees, the relative enthalpies of all the H-shift reactions of the adduct and intermediates, and input files for MESS.

Conflicts of interest

There are no conflicts to declare.

Acknowledgements

This work was supported in part by the National Natural Science Foundation of China (42120104007,41775125, and 91961123), by Guizhou Provincial Science and Technology Projects, China (CXTD [2022]001 and GCC[2023]026), and by the U.S. Department of Energy, Office of Basic Energy Sciences (DE-SC0015997).

Corresponding Authors

*E-mail: wwwltcommon@sina.com (B. Long), haofei.zhang@ucr.edu (H. Zhang), and truhlar@umn.edu (Donald G. Truhlar)

REFERENCES

1 L. Nondek, D. Rodler and J. W. Birks, Measurement of Sub-ppbv Concentrations of Aldehydes in a Forest Atmosphere Using a New HPLC Technique, *Environ. Sci. Technol.*, 1992, **26**, 1174-1178.

2 S. K. Hoekman, Speciated Measurements and Calculated Reactivities of Vehicle Exhaust Emissions from Conventional and Reformulated Gasolines, *Environ. Sci. Technol.*, 1992, **26**, 1206-1216.

3 P. Ciccioli, E. Brancaleoni, M. Frattoni, A. Cecinato and A. Brachetti, Ubiquitous occurrence of semi-volatile carbonyl compounds in tropospheric samples and their possible sources, *Atmos. Environ.*, 1993, **27**, 1891-1901.

4 F. Grimaldi, D. Bacle and A. Viala, Emissions of Carbonyl Compounds from Vehicles Fuelled with Different Gasolines, *Indoor. Environ*, 1995, **4**, 297-301.

5 A. Guenther, C. N. Hewitt, D. Erickson, R. Fall, C. Geron, T. Graedel, P. Harley, L. Klinger, M. Lerdau, W. A. Mckay, T. Pierce, B. Scholes, R. Steinbrecher, R. Tallamraju, J. Taylor and P. Zimmerman, A global model of natural volatile organic compound emissions, *J. Geophys. Res. Atmos*, 1995, **100**, 8873-8892.

6 J. Kesselmeier, K. Bode, U. Hofmann, H. Müller, L. Schäfer, A. Wolf, P. Ciccioli, E. Brancaleoni, A. Cecinato, M. Frattoni, P. Foster, C. Ferrari, V. Jacob, J. L. Fugit, L. Dutaur, V. Simon and L. Torres, Emission of short chained organic acids, aldehydes and monoterpenes from Quercus ilex L. and Pinus pinea L. in relation to physiological activities, carbon budget and emission algorithms, *Atmos. Environ.*, 1997, **31**, 119-133.

7 D. Millet, A. Guenther, D. Siegel, N. Nelson, H. Singh, J. de Gouw, C. Warneke, J. Williams, G. Eerdekens, V. Sinha, T. Karl, F. Flocke, E. Apel, D. Riemer, P. Palmer and M. Barkley, Global atmospheric budget of acetaldehyde: 3-D model analysis and constraints from in-situ and satellite observations, *Atmos. Chem. Phys.*, 2009, **10**, 3405−3425.

8 Y. Li, H. Li, X. Zhang, Y. Ji, R. Gao, Z. Wu, M. Yin, L. Nie, W. Wei, G. Li, Y. Wang, M. Luo and H. Bai, Characteristics, sources and health risk assessment of atmospheric carbonyls during multiple ozone pollution episodes in urban Beijing: Insights into control strategies, *Sci. Total Environ.*, 2023, **863**, 160769.

9 Z. H. Ling, J. Zhao, S. J. Fan and X. M. Wang, Sources of formaldehyde and their contributions to photochemical O_3 formation at an urban site in the Pearl River Delta,

southern China, *Chemosphere.*, 2017, **168**, 1293-1301.
10 M. Jang, N. M. Czoschke, S. Lee and R. M. Kamens, Heterogeneous Atmospheric Aerosol Production by Acid-Catalyzed Particle-Phase Reactions, *Science.*, 2002, **298**, 814-817.
11 A. L. Steiner, R. C. Cohen, R. A. Harley, S. Tonse, D. B. Millet, G. W. Schade and A. H. Goldstein, VOC reactivity in central California: comparing an air quality model to ground-based measurements, *Atmos. Chem. Phys.*, 2008, **8**, 351-368.
12 M. Jang and R. M. Kamens, Atmospheric Secondary Aerosol Formation by Heterogeneous Reactions of Aldehydes in the Presence of a Sulfuric Acid Aerosol Catalyst, *Environ. Sci. Technol.*, 2001, **35**, 4758-4766.
13 R. Atkinson and J. Arey, Atmospheric Degradation of Volatile Organic Compounds, *Chem. Rev.* , 2003, **103**, 4605-4638.
14 S. Vandenberk and J. Peeters, The reaction of acetaldehyde and propionaldehyde with hydroxyl radicals: experimental determination of the primary H_2O yield at room temperature, *J.Photoch.Photobio.A*, 2003, **157**, 269-274.
15 E. Jiménez and I. Barnes, Daytime Atmospheric Chemistry of C_4–C_7 Saturated and Unsaturated Carbonyl Compounds, in *Environment, Energy and Climate Change I*, edited by E. Jiménez, B. Cabañas and G. Lefebvre, Vol. 32 in *The Handbook of Environmental Chemistry*, Springer International Publishing, 2015, pp. 53-103.
16 Y. Zhang, L. Xue, C. Dong, T. Wang, A. Mellouki, Q. Zhang and W. Wang, Gaseous carbonyls in China's atmosphere: Tempo-spatial distributions, sources, photochemical formation, and impact on air quality, *Atmos. Environ.*, 2019, **214**, 116863.
17 H. Hakola, V. Tarvainen, A. Praplan, K. Jaars, M. Hemmilä, M. Kulmala, J. Bäck and H. Hellén, Terpenoid and carbonyl emissions from Norway spruce in Finland during the growing season, *Atmos. Chem. Phys.*, 2017, **17**, 3357-3370.
18 E. Jiménez, B. Lanza, E. Martínez and J. Albaladejo, Daytime tropospheric loss of hexanal and trans-2-hexenal: OH kinetics and UV photolysis, *Atmos. Chem. Phys.*, 2007, **7**, 1565-1574.
19 R. Atkinson and J. N. Pitts, Jr., Kinetics of the reactions of the OH radical with HCHO and CH_3CHO over the temperature range 299-426°K, *J. Chem. Phys.*, 1978, **68**, 3581-3584.
20 M. Mandalakis, H. Berresheim and E. G. Stephanou, Direct Evidence for Destruction of Polychlorobiphenyls by OH Radicals in the Subtropical Troposphere, *Environ. Sci. Technol.*, 2003, **37**, 542-547.
21 I. Faloona, D. Tan, W. Brune, J. Hurst, D. Barket, T. L. Couch, P. Shepson, E. Apel, D. Riemer, T. Thornberry, M. A. Carroll, S. Sillman, G. J. Keeler, J. Sagady, D. Hooper and K. Paterson, Nighttime observations of anomalously high levels of hydroxyl radicals above a deciduous forest canopy, *J. Geophys. Res., Atmos,*, 2001, **106**, 24315-24333.
22 K. M. Emmerson and N. Carslaw, Night-time radical chemistry during the TORCH campaign, *Atmos. Environ.* , 2009, **43**, 3220-3226.
23 D. Stone, L. K. Whalley and D. E. Heard, Tropospheric OH and HO_2 radicals: field measurements and model comparisons, *Chem. Soc. Rev.*, 2012, **41**, 6348-6404.
24 B. Veyret, J. C. Rayez and R. Lesclaux, Mechanism of the photooxidation of formaldehyde studied by flash photolysis of CH_2O-O_2-NO mixtures, *J. Phys. Chem.*, 1982, **86**, 3424-3430.
25 B. Veyret, R. Lesclaux, M. T. Rayez, J. C. Rayez, R. A. Cox and G. K. Moortgat, Kinetics and mechanism of the photo-oxidation of formaldehyde. 1. Flash photolysis study, *J. Phys. Chem.*, 1989, **93**, 2368-2374.
26 J. M. Anglada and V. M. Domingo, Mechanism for the Gas-Phase Reaction between

Formaldehyde and Hydroperoxyl Radical. A Theoretical Study, *J. Phys. Chem. A*, 2005, **109**, 10786-10794.

27 E. M. Evleth, C. F. Melius, M. T. Rayez, J. C. Rayez and W. Forst, Theoretical characterization of the reaction of HO_2 with formaldehyde, *J. Phys. Chem.*, 1993, **97**, 5040-5045.

28 D.-P. Ding and B. Long, Reaction between propionaldehyde and hydroxyperoxy radical in the atmosphere: A reaction route for the sink of propionaldehyde and the formation of formic acid, *Atmos. Environ.*, 2022, **284**, 119202.

29 B. Long, Y. Xia and D. G. Truhlar, Quantitative Kinetics of HO_2 Reactions with Aldehydes in the Atmosphere: High-Order Dynamic Correlation, Anharmonicity, and Falloff Effects Are All Important, *J. Am. Chem. Soc.*, 2022, **144**, 19910-19920.

30 I. Hermans, J.-F. Müller, T. L. Nguyen, P. A. Jacobs and J. Peeters, Kinetics of α-Hydroxy-alkylperoxyl Radicals in Oxidation Processes. $HO_2^{\bullet}$-Initiated Oxidation of Ketones/Aldehydes near the Tropopause, *J. Phys. Chem. A*, 2005, **109**, 4303-4311.

31 P. Morajkar, C. Schoemaecker, M. Okumura and C. Fittschen, Direct Measurement of the Equilibrium Constants of the Reaction of Formaldehyde and Acetaldehyde with HO_2 Radicals, *Int. J. Chem.Kinet*, 2014, **46**, 245-259.

32 I. Barnes, K. H. Becker, E. H. Fink, A. Reimer, F. Zabel and H. Niki, FTIR spectroscopic study of the gas-phase reaction of HO_2 with H_2CO, *Chem. Phys. Lett.*, 1985, **115**, 1-8.

33 G. P. Brasseur and S. Solomon, *Aeronomy of the middle atmosphere: Chemistry and physics of the stratosphere and mesosphere*, Springer Science & Business Media, 2006.

34 J. Lelieveld, S. Gromov, A. Pozzer and D. Taraborrelli, Global tropospheric hydroxyl distribution, budget and reactivity, *Atmos. Chem. Phys.*, 2016, **16**, 12477-12493.

35 J. D. Crounse, L. B. Nielsen, S. Jørgensen, H. G. Kjaergaard and P. O. Wennberg, Autoxidation of Organic Compounds in the Atmosphere, *J. Phys. Chem. Lett.*, 2013, **4**, 3513-3520.

36 T. F. Mentel, M. Springer, M. Ehn, E. Kleist, I. Pullinen, T. Kurtén, M. Rissanen, A. Wahner and J. Wildt, Formation of highly oxidized multifunctional compounds: autoxidation of peroxy radicals formed in the ozonolysis of alkenes – deduced from structure–product relationships, *Atmos. Chem. Phys.*, 2015, **15**, 6745-6765.

37 T. Berndt, S. Richters, T. Jokinen, N. Hyttinen, T. Kurtén, R. V. Otkjær, H. G. Kjaergaard, F. Stratmann, H. Herrmann, M. Sipilä, M. Kulmala and M. Ehn, Hydroxyl radical-induced formation of highly oxidized organic compounds, *Nat. Commun.*, 2016, **7**, 13677.

38 S. Wang, R. Wu, T. Berndt, Mikael Ehn and Liming Wang, Formation of Highly Oxidized Radicals and Multifunctional Products from the Atmospheric Oxidation of Alkylbenzenes, *Environ. Sci. Technol.*, 2017, **51**, 8442−8449.

39 E. Praske, R. V. Otkjær, J. D. Crounse, J. C. Hethcox, B. M. Stoltz, H. G. Kjaergaard and P. O. Wennberg, Atmospheric autoxidation is increasingly important in urban and suburban North America, *Proc. Natl. Acad. Sci.*, 2018, **115**, 64–69.

40 L. Xing, L. Lian, Z. Wang, Z. Cheng, Y. He, J. Cui and D. G. Truhlar, Lowering of Reaction Rates by Energetically Favorable Hydrogen Bonding in the Transition State. Degradation of Biofuel Ketohydroperoxides by OH, *J. Am. Chem. Soc.*, 2022, **144**, 16984-16995.

41 J .Zhao, J. Ortega, M. Chen, P. H. McMurry and J. N. Smith, Dependence of particle nucleation and growth on high-molecular-weight gas-phase products during ozonolysis of α-pinene, *Atmos. Chem. Phys.,* 2013, **13**, 7631–7644.

42 F. Bianchi et al., Highly Oxygenated Organic Molecules (HOM) from Gas-Phase

Autoxidation Involving Peroxy Radicals: A Key Contributor to Atmospheric Aerosol. *Chem. Rev.*, 2019, **119**, 3472−3509.
43 S.-n. Wang, R.-r. Wu and L.-m. Wang, Role of hydrogen migrations in carbonyl peroxy radicals in the atmosphere, *Chinese J. Chem. Phys.*, 2019, **32**, 457-466.
44 S. Barua, S. Iyer, A. Kumar, P. Seal and M. Rissanen, An aldehyde as a rapid source of secondary aerosol precursors: Theoretical and experimental study of hexanal autoxidation, *EGUsphere*, 2023, **2023**, 1-24.
45 X. Qian, H. Shen and Z. Chen, Characterizing summer and winter carbonyl compounds in Beijing atmosphere, *Atmos. Environ.*, 2019, **214**, 116845.
46 W. Chen, M. Shao, M. Wang, S. Lu, Y. Liu, B. Yuan, Y. Yang, L. Zeng, Z. Chen, C.-C. Chang, Q. Zhang and M. Hu, Variation of ambient carbonyl levels in urban Beijing between 2005 and 2012, *Atmos. Environ.*, 2016, **129**, 105-113.
47 Z. Rao, Z. Chen, H. Liang, L. Huang and D. Huang, Carbonyl compounds over urban Beijing: Concentrations on haze and non-haze days and effects on radical chemistry, *Atmos. Environ.*, 2016, **124**, 207-216.
48 J. Bao, H. Li, Z. Wu, X. Zhang, H. Zhang, Y. Li, J. Qian, J. Chen and L. Deng, Atmospheric carbonyls in a heavy ozone pollution episode at a metropolis in Southwest China: Characteristics, health risk assessment, sources analysis, *J. Environ. Sci.*, 2022, **113**, 40-54.
49 F. Li, H. Wang, X. Wang, Z. Xue, L. Duan, Y. Kou, Y. Zhang and X. Chen, Pollution Characteristics of Atmospheric Carbonyls in Urban Linfen in Winter, *Atmos.*, 2020, **11**, 685.
50 J.-H. Xing, M. Ono, A. Kuroda, K. Obi, K. Sato and T. Imamura, Kinetic Study of the Daytime Atmospheric Fate of (Z)-3-Hexenal, *J. Phys. Chem. A*, 2012, **116**, 8523-8529.
51 Q. Liu, Y. Gao, W. Huang, Z. Ling, Z. Wang and X. Wang, Carbonyl compounds in the atmosphere: A review of abundance, source and their contributions to O_3 and SOA formation, *Atmos. Res.*, 2022, **274**, 106184.
52 Y. Zhao and D. G. Truhlar, The M06 suite of density functionals for main group thermochemistry, thermochemical kinetics, noncovalent interactions, excited states, and transition elements: two new functionals and systematic testing of four M06-class functionals and 12 other functionals, *Theor. Chem. Acc.*, 2008, **120**, 215-241.
53 B. J. Lynch, Y. Zhao and D. G. Truhlar, Effectiveness of Diffuse Basis Functions for Calculating Relative Energies by Density Functional Theory, *J. Phys. Chem. A.*, 2003, **107**, 1384-1388.
54 A. D. Isaacson and D. G. Truhlar, Polyatomic canonical variational theory for chemical reaction rates. Separable-mode formalism with application to $OH+H_2 \rightarrow H_2O+H$, 1982, **76**, 1380-1391.
55 T. B. Adler, G. Knizia and H.-J. Werner, A simple and efficient CCSD(T)-F12 approximation, *J. Chem. Phys.*, 2007, **127**, 221106.
56 G. Knizia, T. B. Adler and H.-J. Werner, Simplified CCSD(T)-F12 methods: Theory and benchmarks, *J. Chem. Phys.*, 2009, **130**, 054104.
57 R. Peverati and D. G. Truhlar, M11-L: A Local Density Functional That Provides Improved Accuracy for Electronic Structure Calculations in Chemistry and Physics, *J. Phys. Chem. Lett.*, 2012, **3**, 117-124.
58 H. S. Yu, X. He and D. G. Truhlar, MN15-L: A new local exchange-correlation functional for Kohn–Sham density functional theory with broad accuracy for atoms, molecules, and solids, *J. Chem. Theory Comput.*, 2016, **12**, 1280-1293.
59 I. M. Alecu, J. Zheng, Y. Zhao and D. G. Truhlar, Computational Thermochemistry: Scale

Factor Databases and Scale Factors for Vibrational Frequencies Obtained from Electronic Model Chemistries, *J. Chem. Theory Comput.*, 2010, **6**, 2872-2887.
60 J. Zheng, R. Meana-Pañeda and D. G. Truhlar, Prediction of Experimentally Unavailable Product Branching Ratios for Biofuel Combustion: The Role of Anharmonicity in the Reaction of Isobutanol with OH, *J. Am. Chem. Soc.*, 2014, **136**, 5150-5160.
61 L. G. Gao, J. Zheng, A. Fernández-Ramos, D. G. Truhlar and X. Xu, Kinetics of the Methanol Reaction with OH at Interstellar, Atmospheric, and Combustion Temperatures, *J. Am. Chem. Soc.*, 2018, **140**, 2906-2918.
62 Y. Sun, B. Long and D. G. Truhlar, Unimolecular Reactions of E-Glycolaldehyde Oxide and Its Reactions with One and Two Water Molecules, *Research.*, 2023, **6**, 0143.
63 B. Long, Y. Xia, Y.-Q. Zhang and D. G. Truhlar, Kinetics of Sulfur Trioxide Reaction with Water Vapor to Form Atmospheric Sulfuric Acid, *J. Am. Chem. Soc.*, 2023, **145**, 19866-19876.
64 J. Bloino, M. Biczysko and V. Barone, General Perturbative Approach for Spectroscopy, Thermodynamics, and Kinetics: Methodological Background and Benchmark Studies, *J. Chem. Theory Comput.*, 2012, **8**, 1015-1036.
65 K. M. Kuhler, D. G. Truhlar and A. D. Isaacson, General method for removing resonance singularities in quantum mechanical perturbation theory, *J. Chem. Phys.*, 1996, **104**, 4664-4671.
66 Q. Zhang, P. N. Day and D. G. Truhlar, The accuracy of second order perturbation theory for multiply excited vibrational energy levels and partition functions for a symmetric top molecular ion, *J. Chem. Phys.*, 1993, **98**, 4948-4958.
67 B. J. Lynch, P. L. Fast, M. Harris and D. G. Truhlar, Adiabatic Connection for Kinetics, *J. Phys. Chem. A*, 2000, **104**, 4811-4815.
68 B. Long, J. L. Bao and D. G. Truhlar, Kinetics of the Strongly Correlated $CH_3O + O_2$ Reaction: The Importance of Quadruple Excitations in Atmospheric and Combustion Chemistry, *J. Am. Chem. Soc.*, 2019, **141**, 611-617.
69 B. Long, J. L. Bao and D. G. Truhlar, Atmospheric Chemistry of Criegee Intermediates: Unimolecular Reactions and Reactions with Water, *J. Am. Chem. Soc.*, 2016, **138**, 14409-14422.
70 B. Long, J. L. Bao and D. G. Truhlar, Rapid unimolecular reaction of stabilized Criegee intermediates and implications for atmospheric chemistry, *Nat. Commun.*, 2019, **10**, 2003.
71 X.-F. Tan, B. Long, D.-S. Ren, W.-J. Zhang, Z.-W. Long and E. Mitchell, Atmospheric chemistry of CH_3CHO: the hydrolysis of CH_3CHO catalyzed by H_2SO_4, *Phys. Chem. Chem. Phys.*, 2018, **20**, 7701-7709.
72 X.-F. Tan, L. Zhang and B. Long, New mechanistic pathways for the formation of organosulfates catalyzed by ammonia and carbinolamine formation catalyzed by sulfuric acid in the atmosphere, *Phys. Chem. Chem. Phys.*, 2020, **22**, 8800-8807.
73 B. Long, J. L. Bao and D. G. Truhlar, Unimolecular reaction of acetone oxide and its reaction with water in the atmosphere, *Proc. Natl. Acad. Sci.*, 2018, **115**, 6135-6140.
74 T. Yu, J. Zheng and D. G. Truhlar, Multi-structural variational transition state theory. Kinetics of the 1, 4-hydrogen shift isomerization of the pentyl radical with torsional anharmonicity, *Chem. Sci.*, 2011, **2**, 2199-2213.
75 D. G. Truhlar and B. C. Garrett, Variational transition-state theory, *Acc. Chem. Res.*, 1980, **13**, 440-448.
76 Y. P. Liu, G. C. Lynch, T. N. Truong, D. H. Lu, D. G. Truhlar and B. C. Garrett, Molecular

modeling of the kinetic isotope effect for the [1, 5] sigmatropic rearrangement of cis-1, 3-pentadiene, *J. Am. Chem. Soc.*, 1993, **115**, 2408-2415.
77 Y. Xia, B. Long, A. Liu and D. G. Truhlar, Reactions with criegee intermediates are the dominant gas-phase sink for formyl fluoride in the atmosphere, *Fundamental Research*, 2023, DOI: 10.1016/j.fmre.2023.02.012.
78 S. Glasstone, K. J. Laidler and H. Eyring, The Theory of Rate Processes; McGraw-Hill, New York, , 1941.
79 J. L. Bao, J. Zheng and D. G. Truhlar, Kinetics of Hydrogen Radical Reactions with Toluene Including Chemical Activation Theory Employing System-Specific Quantum RRK Theory Calibrated by Variational Transition State Theory, *J. Am. Chem. Soc.*, 2016, **138**, 2690-2704.
80 J. L. Bao, X. Zhang and D. G. Truhlar, Predicting pressure-dependent unimolecular rate constants using variational transition state theory with multidimensional tunneling combined with system-specific quantum RRK theory: A definitive test for fluoroform dissociation, *Phys. Chem. Chem. Phys.*, 2016, **18**, 16659-16670.
81 J. L. Bao and D. G. Truhlar, Silane-initiated nucleation in chemically active plasmas: validation of density functionals, mechanisms, and pressure-dependent variational transition state calculations, *Phys. Chem. Chem. Phys.*, 2016, **18**, 10097-10108.
82 J. L. Bao, P. Sripa and D. G. Truhlar, Path-dependent variational effects and multidimensional tunneling in multi-path variational transition state theory: rate constants calculated for the reactions of HO_2 with tert-butanol by including all 46 paths for abstraction at C and all six paths for abstraction at O, *Phys. Chem. Chem. Phys.*, 2016, **18**, 1032-1041.
83 J. Zheng and D. G. Truhlar, Quantum Thermochemistry: Multistructural Method with Torsional Anharmonicity Based on a Coupled Torsional Potential, *J. Chem. Theory Comput.*, 2013, **9**, 1356-1367.
84 B. Long, J. L. Bao and D. G. Truhlar, Reaction of SO_2 with OH in the atmosphere, *Phys. Chem. Chem. Phys.*, 2017, **19**, 8091-8100.
85 J. L. Bao and D. G. Truhlar, Variational transition state theory: theoretical framework and recent developments, *Chem. Soc. Rev.*, 2017, **46**, 7548-7596.
86 B. Long, Y. Wang, Y. Xia, X. He, J. L. Bao and D. G. Truhlar, Atmospheric Kinetics: Bimolecular Reactions of Carbonyl Oxide by a Triple-Level Strategy, *J. Am. Chem. Soc.*, 2021, **143**, 8402-8413.
87 K. A. Holbrook, M. J. Pilling and S. H. Robertson, *Unimolecular Reactions, 2nd Edition*, John Wiley & Sons: Chichester, 1996. pp 177- 214.
88 A. Fernández-Ramos, J. A. Miller, S. J. Klippenstein and D. G. Truhlar, Modeling the Kinetics of Bimolecular Reactions, *Chem. Rev.*, 2006, **106**, 4518-4584.
89 Y. Georgievskii, J. A. Miller, M. P. Burke and S. J. Klippenstein, Reformulation and Solution of the Master Equation for Multiple-Well Chemical Reactions, *J. Phys. Chem. A*, 2013, **117**, 12146-12154.
90 S. J. Klippenstein, RRKM Theory and Its Implementation, *Comprehensive Chem. Kinet.*, 2003, **39**, 55-103.
91 C. Eckart, The penetration of a potential barrier by electrons, *Phys. Rev.*, 1930, **35**, 1303-1309.
92 B. C. Garrett and D. G. Truhlar, Semiclassical Tunneling Calculations, *J. Phys. Chem.,* **83**, 2921-2926 (1979).
93 R. L. Brown, A method of calculating tunneling corrections for Eckart potential barriers, *J. Res. Natl. Bur. Stand.*, 1981, **86**, 357-359.
94 W. Forst, The Theory of Unimolecular Reactions, *Academic Press:New York*, 1973, p 190f.

95 J. Zheng, S. L. Mielke, K. L. Clarkson and D. G. Truhlar, MSTor: A program for calculating partition functions, free energies, enthalpies, entropies, and heat capacities of complex molecules including torsional anharmonicity, *Comput. Phys. Commun.*, 2012, **183**, 1803-1812.

96 J. Zheng, R. Meana-Pañeda and D. G. Truhlar, MSTor version 2013: A new version of the computer code for the multi-structural torsional anharmonicity, now with a coupled torsional potential, *Comput. Phys. Commun.*, 2013, **184**, 2032-2033.

97 J. Zheng, S. L. Mielke, J. L. Bao, R. Meana-Pañeda, K. L. Clarkson and D. G. Truhlar, MSTor-version 2017; University of Minnesota: 1077 Minneapolis, M., 2017. https://t1.chem.umn.edu/mstor/ update.htm1078 (accessed May 5, 2017).

98 M. J. Frisch, G. W. Trucks, H. B.Schlegel, G. E. Scuseria, M. A. Robb, J. R. Cheeseman, G. Scalmani, V. Barone, G. A.Petersson, H. Nakatsuji, X. Li, M. Caricato, A. V. Marenich, J. Bloino, B. G. Janesko, R. Gomperts, B. Mennucci, H. P. Hratchian, J. V. Ortiz,; A. F. Izmaylov, J. L. Sonnenberg, D. Williams-Young, F. Ding, F. Lipparini, F. Egidi, J. Goings, B. Peng, A. Petrone, T. Henderson, D. Ranasinghe, V. G. Zakrzewski, J. Gao, N. Rega, G.Zheng, W. Liang, M. Hada, M. Ehara, K. Toyota, R. Fukuda,; J. Hasegawa, M. Ishida, T. Nakajima, Y. Honda, O. Kitao, H. Nakai, T. Vreven, K. Throssell, J. A. Montgomery Jr, , J. E. Peralta, F. Ogliaro, M. Bearpark, J. J. Heyd, E. Brothers, K. N. Kudin, V. N. Staroverov, T. A. Keith, R. Kobayashi, J. Normand, K. Raghavachari, A. P. Rendell, J. C. Burant, S. S. Iyengar, J. Tomasi, M. Cossi, J. M. Millam, M. Klene, C. Adamo, R. Cammi, J. W. Ochterski, R. L. Martin, K. Morokuma, O. Farkas, J. B. Foresman and D. J. Fox, Gaussian 16, Revision B.01; Gaussian, Inc.: Wallingford, CT, 2016.

99 H.-J. Werner, P. J. Knowles, G. Knizia, F. R. Manby, M. Schütz, P. Celani, W. Györffy, D. Kats, T. Korona, R. Lindh, A. Mitrushenkov, G. Rauhut, K. R. Shamasundar, T. B. Adler, R. D. Amos, S. J. Bennie, A. Bernhardsson, A. Berning, D. L. Cooper, M. J. O. Deegan, A. J. Dobbyn,; F. Eckert, E. Goll, C. Hampel, A. Hesselmann, G. Hetzer, T. Hrenar, G. Jansen, C. Köppl, S. J. R.Lee, Y. Liu, A. W. Lloyd, Q. Ma, R. A. Mata, A. J. May, S. J. McNicholas, W. Meyer, T. F. Miller, M. E. Mura, A. Nicklaß, D. P. O'Neill, P. Palmieri, D. Peng, K. Pflüger, R. Pitzer, M. Reiher, T. Shiozaki, H. Stoll, A. J. Stone, R.Tarroni, T. Thorsteinsson and M. Wang, Welborn, M.Molpro 2019.2, a package of ab initio programs. See https://www.molpro.net.

100 J. Zheng, L. J. W. Bao, R. Meana-Pan˜eda, S. Zhang, B. J. Lynch, J. C. Corchado, Y.-Y. Chuang, P. L. Fast, W.-P. Hu, Y.-P. Liu, G. C. Lynch, K. A. Nguyen, C. F. Jackels, A. Fernandez Ramos, B. A. Ellingson, V. S. Melissas, J. Villa, I. Rossi, L. Coitino, J. Pu, T. V. Albu, R. Steckler, B. C. Garrett, A. D. Issacson and D. G. Truhlar, Polyrate – version 2017-C, University of Minnesota, Minneapolis, 2018.

101 J. Zheng, L. J. W. Bao, S. Zhang, J. C. Corchado, Y.-Y. Chuang, E. L. Coitin˜o, B. A. Ellingson and D. G. Truhlar, Gaussrate– version 2017-B, University of Minnesota, Minneapolis, 2018.

102 Y. Georgievskii, S. J. Klippenstein. MESS. http://tcg.cse.anl. gov/papr/codes/mess.html (accessed May 1, 2019)

103 Z. Zhao, W. Zhang, T. Alexander, X. Zhang, D. B. C. Martin and H. Zhang, Isolating α-Pinene Ozonolysis Pathways Reveals New Insights into Peroxy Radical Chemistry and Secondary Organic Aerosol Formation, *Environ. Sci. Technol.*, 2021, **55**, 6700-6709.

104 R. Mayorga, Y. Xia, Z. Zhao, B. Long and H. Zhang, Peroxy Radical Autoxidation and Sequential Oxidation in Organic Nitrate Formation during Limonene Nighttime Oxidation,

Environ. Sci. Technol., 2022, **56**, 15337-15346.
105 A. T. Lambe, J. Zhang, A. M. Sage and N. M. Donahue, Controlled OH Radical Production via Ozone-Alkene Reactions for Use in Aerosol Aging Studies, *Environ. Sci. Technol.*, 2007, **41**, 2357-2363.
106 W. Zhang and H. Zhang, Secondary Ion Chemistry Mediated by Ozone and Acidic Organic Molecules in Iodide-Adduct Chemical Ionization Mass Spectrometry, *Anal. Chem.*, 2021, **93**, 8595-8602.
107 Z. Zhao, R. Tolentino, J. Lee, A. Vuong, X. Yang and H. Zhang, Interfacial Dimerization by Organic Radical Reactions during Heterogeneous Oxidative Aging of Oxygenated Organic Aerosols, *J. Phys. Chem. A*, 2019, **123**, 10782-10792.
108 B. H. Lee, C. Mohr, F. D. Lopez-Hilfiker, A. Lutz, M. Hallquist, L. Lee, P. Romer, R. C. Cohen, S. Iyer, T. Kurtén, W. Hu, D. A. Day, P. Campuzano-Jost, J. L. Jimenez, L. Xu, N. L. Ng, H. Guo, R. J. Weber, R. J. Wild, S. S. Brown, A. Koss, J. de Gouw, K. Olson, A. H. Goldstein, R. Seco, S. Kim, K. McAvey, P. B. Shepson, T. Starn, K. Baumann, E. S. Edgerton, J. Liu, J. E. Shilling, D. O. Miller, W. Brune, S. Schobesberger, E. L. D'Ambro and J. A. Thornton, Highly functionalized organic nitrates in the southeast United States: Contribution to secondary organic aerosol and reactive nitrogen budgets, *Proc. Natl. Acad. Sci. U.S.A.*, 2016, **113**, 1516-1521.
109 S. Iyer, X. He, N. Hyttinen, T. Kurtén and M. P. Rissanen, Computational and Experimental Investigation of the Detection of HO_2 Radical and the Products of Its Reaction with Cyclohexene Ozonolysis Derived RO_2 Radicals by an Iodide-Based Chemical Ionization Mass Spectrometer, *J. Phys. Chem. A*, 2017, **121**, 6778-6789.
110 C. Mohr, F. D. Lopez-Hilfiker, T. Yli-Juuti, A. Heitto, A. Lutz, M. Hallquist, E. L. D'Ambro, M. P. Rissanen, L. Hao, S. Schobesberger, M. Kulmala, R. L. Mauldin III, U. Makkonen, M. Sipilä, T. Petäjä and J. A. Thornton, Ambient observations of dimers from terpene oxidation in the gas-phase: Implications for new particle formation and growth, *Geophys. Res. Lett.*, 2017, **44**, 2958-2966.
111 X. Zhang, A. T. Lambe, M. A. Upshur, W. A. Brooks, A. Gray Bé, R. J. Thomson, F. M. Geiger, J. D. Surratt, Z. Zhang, A. Gold, S. Graf, M. J. Cubison, M. Groessl, J. T. Jayne, D. R. Worsnop and M. R. Canagaratna, Highly Oxygenated Multifunctional Compounds in α-Pinene Secondary Organic Aerosol, *Environ. Sci. Technol.*, 2017, **51**, 5932-5940.
112 J. Zheng, R. Meana-Pañeda and D. G. Truhlar, Prediction of Experimentally Unavailable Product Branching Ratios for Biofuel Combustion: The Role of Anharmonicity in the Reaction of Isobutanol with OH, *J. Am. Chem. Soc.*, 2014, **136**, 5150-5160.
113 J. Zheng, G. A. Oyedepo and D. G. Truhlar, Kinetics of the Hydrogen Abstraction Reaction From 2-Butanol by OH Radical, *J. Phys. Chem. A*, 2015, **119**, 12182-12192.
114 R. Meana-Pañeda, X. Xu, H. Ma and D. G. Truhlar, Computational Kinetics by Variational Transition-State Theory with Semiclassical Multidimensional Tunneling: Direct Dynamics Rate Constants for the Abstraction of H from CH_3OH by Triplet Oxygen Atoms, *J. Phys. Chem. A*, 2017, **121**, 1693-1707.
115 L. G. Gao, J. Zheng, A. Fernández-Ramos, D. G. Truhlar and X. Xu, Kinetics of the Methanol Reaction with OH at Interstellar, Atmospheric, and Combustion Temperatures, *J. Am. Chem. Soc.*, 2018, **140**, 2906-2918.
116 L. G. Gao, D. G. Fleming, D. G. Truhlar and X. Xu, Large Anharmonic Effects on Tunneling and Kinetics: Reaction of Propane with Muonium, *J. Phys. Chem. Lett.*, 2021, **12**, 4154-4159.
117 J. Zheng and D. G. Truhlar, Multi-path variational transition state theory for chemical

reaction rates of complex polyatomic species: ethanol + OH reactions, *Faraday Discuss.*, 2012, **157**, 59-88.

118 J. L. Bao, R. Meana-Pañeda and D. G. Truhlar, Multi-path variational transition state theory for chiral molecules: The site-dependent kinetics for abstraction of hydrogen from 2-butanol by hydroperoxyl radical, analysis of hydrogen bonding in the transition state, and dramatic temperature dependence of the activation energy, *Chem. Sci.*, 2015, **6**, 5866-5881.

119 L. Vereecken and B. Nozière, H migration in peroxy radicals under atmospheric conditions, *Atmos. Chem. Phys.*, 2020, **20**, 7429-7458.

120 W. Zhao, B. Fang, X. Lin, Y. Gai, W. Zhang, W. Chen, Z. Chen, H. Zhang and W. Chen, Superconducting-Magnet-Based Faraday Rotation Spectrometer for Real Time in Situ Measurement of OH Radicals at 10^6 Molecule/cm^3 Level in an Atmospheric Simulation Chamber, *Anal. Chem.*, 2018, **90**, 3958-3964.

121 M. A. H. Khan, M. J. Ashfold, G. Nickless, D. Martin, L. A. Watson, P. D. Hamer, R. P. Wayne, C. E. Canosa-Mas and D. E. Shallcross, Night-time NO_3 and OH radical concentrations in the United Kingdom inferred from hydrocarbon measurements, *Atmosph. Sci. Lett.*, 2008, **9**, 140-146.

122 D. Asaf, E. Tas, D. Pedersen, M. Peleg and M. Luria, Long-Term Measurements of NO_3 Radical at a Semiarid Urban Site: 2. Seasonal Trends and Loss Mechanisms, *Environ. Sci. Technol.*, 2010, **44**, 5901-5907.

123 Y. Ren, L. Zhou, A. Mellouki, V. Daële, M. Idir, S. S. Brown, B. Ruscic, R. S. Paton, M. R. McGillen and A. R. Ravishankara, Reactions of NO_3 with aromatic aldehydes: gas-phase kinetics and insights into the mechanism of the reaction, *Atmos. Chem. Phys.*, 2021, **21**, 13537-13551.

124 C. Papagni, J. Arey and R. Atkinson, Rate constants for the gas-phase reactions of a series of C3-C6 aldehydes with OH and NO_3 radicals, *Int. J. Chem. Kinet.*, 2000, **32**, 79-84.